

ADDRESSING ENGINEERING CHALLENGES IN BIOACOUSTIC RECORDING

A Dissertation

Presented to the Faculty of the Graduate School

of Cornell University

In Partial Fulfillment of the Requirements for the Degree of

Doctor of Philosophy

by

Peter M. Marchetto

May 2015

© 2015 Peter M. Marchetto

ADDRESSING ENGINEERING CHALLENGES IN BIOACOUSTIC RECORDING

Peter M. Marchetto, Ph. D.

Cornell University 2015

Bioacoustics is a very challenging field due to the necessity of putting fragile, power-hungry pieces of instrumentation out in isolated, hostile environments for long periods of time. Making these instruments as durable as possible, while also considering weight, power consumption, size, and affordability is a constant struggle. In this dissertation, multiple engineering challenges associated with these environments are addressed.

BIOGRAPHICAL SKETCH

Peter Marchetto earned his Bachelor of Science degree from Ramapo College of New Jersey in 2007, and his Master of Science degree upon his successful completion of the A exam at Cornell University in 2015.

Before any of that, he began his life in research by working in the applied physics and biomedical engineering lab of Dr. Gordon Thomas at NJIT on biomedical instrumentation calibration. From there, he worked under Dr. Robert Fechtner as a research assistant in the ophthalmology department at UMDNJ, helping with tonometry and laser tomography studies. After that, he turned his attention to the strange anti-resonant behaviors of the Metglas family of magnetostrictive amorphous metal alloys under Dr. Philip Anderson at RCNJ.

After graduating with his BS, he moved on to work for a calibration company in State College, PA, writing and performing calibration procedures, then a genomics software company in the same town, implementing a QA/QC program for them for the first time. From here he moved on to studying ferroelectric polymers and their piezoelectric and dielectric properties at the Penn State Materials Research Lab as a visiting scientist.

Peter has been at Cornell University, first as a staff member since 2009, then also as a graduate student through the Employee Degree Program since 2010, in the Bioacoustics Research Program at the Cornell Lab of Ornithology. Since 2014 he has also been a member of the Soil and Water Lab, doing instrumentation design for their experiments. Since coming to Cornell, he has been focused on design challenges relating to the placement of recording and logging instruments in harsh environments, the very work that this dissertation hopes to address.

For Katie

ACKNOWLEDGMENTS

Those to whom I owe a great debt of gratitude for their help during the last several years would make a list greater than the length of this entire document, so I'll try to be concise. First of all, I'd like to thank my committee for encouraging me and helping me to bring this work to fruition. I'd like to thank Harold Cheyne for being a fantastic mentor for the last nearly six years, Chris Clark for being an absolute inspiration about what it means to be an engineer working in the biosciences, David "Wink" Winkler for his wonderfully encouraging talks with me, and of course my advisor, Todd Walter, for taking me on as a grad student kind of at the last minute and pushing me to finish with a gentle but firm and humorous hand.

Thanks also to the Cornell Employee Degree Program for funding my tuition.

My thanks also to the two people responsible for getting me started in the graduate program: Wolfgang Sachse and Dan Aneshansley. I'd also thank my advisors in my previous institutions. Gordon Thomas at NJIT is single-handedly responsible for getting me started in physics and instrumentation research (not to mention introducing me to liquid nitrogen). Similarly, Phil Anderson at RCNJ is responsible for helping me to become a researcher, and for guiding my progress in experimental physics.

My co-workers at the Lab of Ornithology also deserve a great deal of credit, especially my compatriots in engineering and deployment: Rob Koch, Adam Strickhart, Karl Fitzke, Rob MacCurdy, Sherwood Snyder, Ed Moore, and Rich Gabrielson to name a few. The two that stand out the most are Chris Tessaglia-Hymes and Ray Mack: without their encouragement, support, and open doors, ears, and minds, this work would not have taken form.

Finally, I'd like to thank my family: my parents Nancy and Pete Marchetto, my in-laws, John, Caroline, and Matt Myers, and Dan and April Bupp, for understanding when deadlines loomed and for always being interested in my progress. Most

importantly, though, I'd like to thank my wife, Katie, without whom I never would've moved to Ithaca, started in the PhD program, or undertaken many of the other prerequisites to this document's existence; truly she is the unseen hand holding mine throughout all of my work, the best biologist I've ever collaborated with, and the love of my life.

Thank you all so much.

TABLE OF CONTENTS

Biographical Sketch	iv
Acknowledgements	vi
List of Figures	ix
List of Tables	x
List of Abbreviations	xi
List of Symbols	xii
Preface	xiii
Temperature Compensation of a Quartz Tuning-Fork Clock Crystal via Post-Processing	1
Use of Cosmic Ray Air Shower Products for Synchronization of Underwater Recording Units	12
Motion in the Ocean: The dynamics of sinking and rising objects through current levels	19
Characterization of marine autonomous recording units	26
The Sound Pressure Level Observing Transponder (SPLOT): a satellite-enabled sensor package for near real time monitoring	34
References	43

LIST OF FIGURES

1.1 Localization Comparison	7
1.2 $f(T)$ Fitted Curve	8
2.1 Detector Circuit	15
2.2 Candidate Events	16
2.3 Fine Resolution Candidate Events	16
2.4 Uncorrected Clock Drift	17
2.5 Detections and Offsets	17
3.1 Drift Phase Diagram	21
3.2 Displacement and Search Area	25
4.1 Analog Signal Chain	28
4.2 Rail Voltage	29
4.3 Test System Diagram	31
4.4 Tests System State Diagram	31
4.5 Sample $f(T)$ Curve	32
4.6 Sample Response Curves	33
5.1 SPLOT Block Diagram	37
5.2 SPLOT State Diagram	38
5.3 GPS Uncertainty	40
5.4 Sheep Track	40
5.5 Comparison of Trends	41

LIST OF TABLES

1.1 Average Absolute Sync	9
1.2 Average Relative Sync	9
3.1 Input Parameters	20
3.2 Output Variables	20
5.1 Measurement Uncertainties	39
5.2 Measurement Units and Precisions	39

LIST OF ABBREVIATIONS

MARU	Marine Autonomous Recording Unit
SPLOT	Sound Pressure Level Observing Transponder
SPL	Sound Pressure Level (dB re 20 μ Pa in air or 1 μ Pa in water)
RH	Relative Humidity
CLO	Cornell Lab of Ornithology
BRP	Bioacoustics Research Program
TDoA	Time Delay of Arrival

LIST OF SYMBOLS

f	Frequency (Hz)
T	Temperature (°C)
k	Coefficient (units variable)
E	Energy (J)
r, ℓ, a, b	Radius or linear distance (m)
V	Electrical potential (V) or Volume (L)
Y	Young's modulus (Pa)
ω	Angular velocity (°/sec or rad/sec)
ϵ	Permittivity (F/m)
N	Population (integer number)
C	Carryover constant (real number)
P	Pressure (Pa)
M	Sensitivity (V/Pa)
c_d	Drag coefficient (unitless)
ρ	Density (kg/L)
t	Time (sec)
h	Depth (m, z-axis only)
v	Velocity (m/sec)
A	Area (m ²)
τ	Time constant (sec)
g	Gravity (9.81 m/sec ²)
θ	Angle (° or rad)

PREFACE

There are two things that one can be certain of when placing recording devices in the outdoors: not all of them will come back unscathed, and not all of them will function as planned. In between the times when they're placed and retrieved, these can go through some strange conditions, which is especially true of marine recording devices. During placement, they can drift with currents. While sitting at depth, they can chill down to temperatures that affect the uniformity of their sample clocks. Over time, their components can age at different rates, and there's always the chance of variability from unit to unit of sensitivity. There's also a need to measure environmental variables in the context of noise level so as to find out what the properties of the medium through which sound is traveling are.

Another problem is that of localization: when trying to use Time Delay of Arrival (TDoA) methods to ascertain the origin of a signal across an array of receivers, several sources of uncertainty crop up. The first, and largest of these, is that of clock drift. As stated above, recorders are usually in variable temperature environments, and so wind up with a large temperature-induced shift in clock rate. This can be on the order of several Hz, which seems small compared to clock frequencies in the tens of kHz, but when the recorder is shy a few Hz for several months, temporal drifts in the recording on the order of minutes may occur, and these drifts will not be uniform across an array of recorders. This induces a TDoA error on the order of km. The second order error is that of acoustic multipath error. This is usually on the order of a few wavelengths, and occurs when reflection or refraction occurs in the signal path, and can lead to several tens or hundreds of meters. Finally, at the third order, mechanical drifting during sinking from the deployment point of a recorder due to an in-water current is responsible for errors on the order of several tens or hundreds of meters, but in a specific direction.

In the papers that follow, all of the aforementioned ideas are addressed. Under the overarching theme stated in the title of engineering challenges in this area, these five papers begin to give some idea of how to address some of the largest problems in this field today.

In the first paper, “Temperature compensation of a quartz tuning-fork clock crystal via post-processing,” a compensation algorithm addresses temperature-induced frequency drift in a sample clock of a recording device. This algorithm takes as its input the fitted curve of $f(T)$, the frequency-temperature dependence function. This function is defined by cooling a clock while recording the frequency that it’s operating at, then warming it back up, and finally fitting a quadratic curve to the resultant data. This paper has been published in the Proceedings of the IEEE IFCS conference, a peer-reviewed proceedings journal.

The second paper, “Use of Cosmic Ray Air Shower Products for Synchronization of Underwater Recording Units,” makes use of the ground-penetrating nature of cosmic rays to propose a means of synchronizing an array of recorders sitting in an RF-inaccessible location, like the bottom of the ocean. These cosmic rays, along with the fast subatomic particles that they create during interactions in the atmosphere, ground, and water, create a signal that can be seen easily by two recorders in an array, and which propagates at the same rate as the sample rate of the recorders. Thus, a signal picked up by two recorders can be used to anchor them in time to one another, and signals picked up across an array can be used through cross-correlation to align the timing of recordings from the entire array. This paper is being submitted to the journal Review of Scientific Instruments.

The third paper, “Motion in the Ocean: The dynamics of sinking and rising objects through current levels,” addresses another kind of drift. In this case, this is the mechanical drift caused by oceanic sub-surface currents, which induce a significant

uncertainty into the latitude and longitude of the location of a recorder on the seafloor. This paper has been submitted to the Ocean Modeling.

Fourth in the list of papers is “Characterization of Marine Autonomous Recording Units (MARUs),” a characterization protocol paper. This paper describes exactly how to characterize an underwater recording unit, and makes suggestions on how to use the characterization data to calibrate the acoustic data returned from the recorder. This paper has been submitted to the Journal of the Acoustical Society of America-Express Letters.

The final paper of this group, “The Sound Pressure Level Observing Transponder (SPLOT): A Satellite-Enabled Sensor Package For Near Real Time Monitoring,” is a description of a proof-of-concept experiment in getting ambient noise levels and all of the parameters needed to calculate acoustic impedance back from the field via satellite modem. The experiment was a success, as the paper shows, and the design itself is viable and useful. This paper has been submitted to the Transactions of the American Society of Agricultural and Biological Engineers.

By looking deeply into the engineering challenges facing bioacousticians and anyone else who would record data in these harsh environments, solutions can be found to improve recorders, and to create smaller uncertainties in the resultant data. Furthermore, careful design based on the results of these studies will allow for more devices to come back unscathed, functioning as planned, with more data that can be of use to those doing the recording.

Temperature Compensation of a Quartz Tuning-Fork Clock Crystal via Post-Processing

Peter Marchetto*, Adam Strickhart, Raymond Mack, and Harold Cheyne

Bioacoustics Research Program, Cornell Lab of Ornithology

Cornell University

Ithaca, NY

*pmm223@cornell.edu

Abstract— The dependence of a tuning-fork quartz crystal oscillator’s frequency f on temperature T is observed over the temperature range -5 to 20°C . From this, a parabolic $f(T)$ function is fit to the crystal’s data, and used to compensate for sampling period drift in an Analog to Digital Converter (ADC) system based around this crystal at various temperatures. Resolution and uncertainty of this method are discussed.

I. INTRODUCTION

A tuning-fork quartz crystal oscillator is one of a family of devices that vibrate at a given frequency when invested with energy by way of an electric field. However, internal mechanical stresses coupled with the device's thermal expansion and contraction cause this frequency to vary with temperature. The variation can be roughly characterized by a parabolic function, $f(T)$, such

that $f(T)=k_1T^2+k_2T+k_3$. Each crystal is designed with a stability temperature, T_0 , and corresponding frequency f_0 , near which small changes in temperature result in small changes in frequency. Most commercially available crystals have a T_0 at around room temperature (20 ± 2 °C). Operation at temperatures far from T_0 results in increasing deviations from f_0 . When such a crystal is used to generate the sampling clock for an ADC at temperatures far from T_0 , the sampling rate will be inaccurate by the same factor. Existing methods used to minimize the temperature dependence of the oscillator include (a) heating it to T_0 , known as furnacing the crystal; (b) cutting the crystal such that its T_0 is at the target temperature for operation; or (c) cutting the crystal to create a flatter $f(T)$ function – that is, minimizing k_1 and k_2 .

Disadvantages of these methods are that furnacing is power intensive, while custom crystal cutting for flat $f(T)$ or target T_0 is cost prohibitive for most applications, and does not compensate for additional temperature variations. A data acquisition platform used by our group (the Marine Autonomous Recording Unit, or MARU[1]) typically operates near 0°C for months at a time, resulting in the accumulation of several minutes of sampling period drift. Additionally its power and cost budgets are limited, making furnaced or custom-cut crystals infeasible. Using characteristic $f(T)$ curves for the MARU’s crystal, in conjunction with data on its temperature over time, we developed a method to minimize the frequency error and were able to demonstrate reduction in sampling period drift as it pertains to acoustically-derived location estimates.

II. THEORETICAL BACKGROUND

The mode of the oscillator in question is flexural, in the xy -plane. The energy of the system is equivalent to the sum of the thermal energy, E_T , the electrical energy, E_E , and the mechanical energy of the oscillator, E_M . The last term is also temperature dependent, such that

$$\Sigma E = E_T + E_\varepsilon + E_M = k_B T + \frac{\varepsilon}{2} \left| \frac{V(t)}{r(t)} \right|^2 + \frac{Y}{ab\ell} r^2(t) \left(\frac{\pi \frac{a}{\sqrt{12}}}{8\ell^2} \right)^2. \quad (1)$$

Where k_B is Boltzmann's constant, T is the temperature in Kelvins, ε is the electric permittivity, $V(t)$ is the voltage at time t , $r(t)$ is the distance between the two tines of the tuning fork at time t , Y is the Young's modulus of the material, a is the thickness of the tines in the flexural plane (i.e. $\hat{a} = \hat{r}$), b is the thickness of the tines through the flexural plane (i.e. $\hat{b} \perp \hat{r}$), and ℓ is the length of the tines (i.e. $\hat{\ell} \perp \hat{r}$ and $\hat{\ell} \perp \hat{b}$)[2].

However, while the temperature dependence in this expression may seem small in magnitude, it is key to remember that r , Y , a , b , and ℓ are all temperature dependent, and thus should be stated as $Y(T)$, $a(T)$, $b(T)$, $\ell(T)$, and $r(t, T)$, respectively. Thus, these could be stated by the following:

$$\begin{aligned} Y(T) &= Y_0 - Y_T T^{-T_\alpha/T} \\ a(T) &= a_0(\alpha\Delta T + 1) \\ b(T) &= b_0(\alpha\Delta T + 1) \\ \ell(T) &= \ell_0(\alpha\Delta T + 1) \\ r(t, T) &= \sin(\omega(T)t)\ell(T) + r_0(\alpha\Delta T + 1) \end{aligned} \quad (2)$$

Where Y_0 is the Young's modulus at absolute zero, Y_T is the Young's modulus at high temperatures (i.e. room temperature of 20 ± 2 °C), $e^{-T_\alpha/T}$ is the Boltzmann factor, α is the linear thermal expansion coefficient, a_0 , b_0 , and ℓ_0 are the theoretical lengths in the three dimensions of the object at absolute zero, $\omega(T)$ is the reduced frequency such that $\omega(T) = \frac{f(T)}{2\pi}$, at a given temperature, and r_0 is the theoretical separation between the tines at absolute zero. [2], [3]

Furthermore, the permittivity, ε , is affected by temperature, and is anisotropic within the oscillator. Given the complexity of this factor, it shall be expressed merely as $\varepsilon(T)$. This affects the total energy thus:

$$\Sigma E = k_B T + \frac{\varepsilon(T)}{2} \left| \frac{V(t)}{\sin(\omega(T)t)\ell_0(\alpha\Delta T + 1) + r_0(\alpha\Delta T + 1)} \right|^2 + \frac{Y_0 - Y_T T^{-T_0/T}}{a_0 b_0 \ell_0 (\alpha\Delta T + 1)^3} (\sin(\omega(T)t)\ell_0(\alpha\Delta T + 1) + r_0(\alpha\Delta T + 1))^2 \left(\frac{\pi a_0 (\alpha\Delta T + 1)}{\sqrt{12}} \right) \left(\frac{\pi}{8(\ell_0(\alpha\Delta T + 1))^2} \right) \quad (3)$$

All three terms have a temperature dependence. At T_0 , the three terms are balanced such that the mechanical term dominates. At lower temperatures, where there is less energy overall, the electrical term dominates, and at higher temperatures, where $Y(T)$ is minimized, and the material becomes more mechanically compliant, the thermal and electrical terms dominate. Since the mechanical resonance of the tuning fork is most efficient at T_0 , the surprising result from this theoretical analysis is that, indeed, the system will follow a parabolic temperature response.

III. METHODS

Implementing temperature correction of frequency based on this model takes place in four phases. The first phase is the characterization the $f(T)$ function for the crystal oscillator. The second is datalogging the temperature of the oscillator during the period requiring correction. The third is the combination of the temperature log and the $f(T)$ function into a frequency-drift profile for that period. The final stage is the application of the frequency-drift profile to the data recorded in that period. The first phase requires measurement of the crystal's oscillation rate over a range of temperatures. This range must include any temperature to which the crystal might be exposed during its use.

The clock crystals in our testing were part of ADC boards (Tattletale Model 8, Onset Computer Corp, Pocasset, MA). The crystals were used along with a low-power oscillator (HA7210, Intersil Corp., Milpitas, CA) with a temperature stability of 0.1 ppm/°C. A 14 VDC rail and a ground rail were attached to eight of the ADC boards on a mounting fixture. The temperature of each crystal was taken by a thermocouple input to a USA thermometer board (Model 1048,

Phidgets, Inc., Calgary, AB). The 40 kHz clock output of the ADC boards was input to a DMM in frequency counting mode (34410A, Agilent Technologies, Inc., Santa Clara, CA) through a signal relay board (Model 1048, Phidgets, Inc., Calgary, AB). A virtual instrument created in LabView (National Instruments, Austin, TX) was used to log data from the $f(T)$ curve, and was also used to control the system using the relay board.

The ADCs were attached to the mounting fixture, and the program started. The first few readings were taken at room temperature (~ 20 °C), then the fixture was lowered into a freezer (Model FFFC05M2KW, Frigidaire, Martinez, GA) and remained there until its temperature stabilized around -10 ± 2 °C. At this point, it was removed and allowed to return to room temperature, in order to characterize system hysteresis.

The second phase of the process requires measurement and recording of the crystal's temperature over the course of the correction period. The measurement interval should be based on the expected rate of temperature change of the crystal and on any implementation specifics of the temperature datalogger, including the temperature datalogger's own temperature and timing uncertainties. The second phase was executed as follows in our implementation.

The characterized ADC board was installed in a MARU. A digital temperature logger (Hobo U23 Pro V2 external Temperature Data Logger, Onset Computer Corp., Pocasset, MA) was installed next to it. Directly attaching the temperature probe to the crystal was not feasible given the electronics layout, but the thermal mass of the system was great enough to eliminate the risk of persistent or transient temperature gradients within the MARU. Additionally, the electronics surrounding the crystal are low enough power that self-heating was not significant. The temperature datalogger was set to a sampling interval of 15 minutes and activated just prior to the sealing of the MARU. This interval took into account the datalogger's battery capacity and

storage space, granting three years of battery life and fourteen months of storage life. This covered the majority of use cases of the MARU. The 15-minute interval was at least twice as long as the expected accumulated frequency-drift of the clock crystal over a standard deployment (90 days), ensuring that the correction factor applied to the recording would never deviate by more than one interval. Because the thermal mass of the MARU is high, even 20°C changes in air-to-water temperature at deployment took over 8 hours to propagate throughout the MARU. This ensured that temperature values taken every 15 minutes adequately described the temperature changes experienced by the crystal. At deployment, the MARU itself was activated and configured to record audio and placed in the water. At recovery, the MARU was pulled from the water and deactivated. The temperature datalogger continued to sample the temperature in the MARU, throughout the entire recording period. After the MARU was returned to the lab, it was unsealed, and the audio recording and temperature datalogger were removed for processing. The third phase generates a frequency-drift profile over the correction period. Giving the temperature time series as input to the $f(T)$ function gives the modeled frequencies vs. time. These can be compared to f_0 to calculate the error in each interval and over the whole correction period. Depending on the nature of the data recorded during this period, an alternate method of expressing the effect of drift may be appropriate. The third phase was implemented for our case as follows: In the lab, the temperature record was extracted from the datalogger and saved in a generic Comma-Separated-Value format (.CSV). The temperature data were then copied into and processed using a Microsoft Excel 2007 macro-enabled spreadsheet to generate a temperature-correction profile over time for the recording. The spreadsheet tool used information from the deployment configuration to calculate the correction factors, primarily the temperature model function $f(T)$ for the ADC board used in the MARU. The tool used the sampling rate of the

audio recording to properly scale the frequency drift of the crystal. It used the time zone information for the temperature datalogger and audio recording start times to correct for deployments that occur around the world or that span daylight savings changes. The output of the tool was a .CSV file that contains the start time of the temperature time series in the time zone of the audio recording, and a listing of time intervals and number of missing or extra audio samples in that interval. The corrective sample counts were calculated as follows:

$$\begin{aligned}
 N &= t_i \frac{f_s - f_s f(T_i)}{f_c} + C \\
 &= t_i \frac{f_s - f_s(k_1 T_i^2 + k_2 T_i + k_3)}{f_c} + C
 \end{aligned} \quad (4)$$

(1) Where N is the sample count, t_i was the interval duration in seconds, f_s was the desired sampling rate of the audio recording in Hz, T_i was the measured temperature for the interval in degrees Celsius, f_c was the theoretical frequency of the crystal at T_0 in Hz, C was an accumulated correction factor in samples which is discussed below, and k_1 , k_2 , and k_3 were the quadratic coefficients of the frequency drift model in $\text{Hz}/^\circ\text{C}^2$, $\text{Hz}/^\circ\text{C}$, and Hz , respectively. In general N was not an integer value, so to correct for this N was rounded to the nearest integer, and a running tally of the error that this introduced was kept. Whenever the absolute value of the tally exceeded one, that sample was removed from the tally and added to or subtracted from the current interval's sample count. This correction factor kept the sub-sample error over the entire temperature profile less than one. Both the rounding and the sample accumulation were accounted for in the C term of Eq. (4).

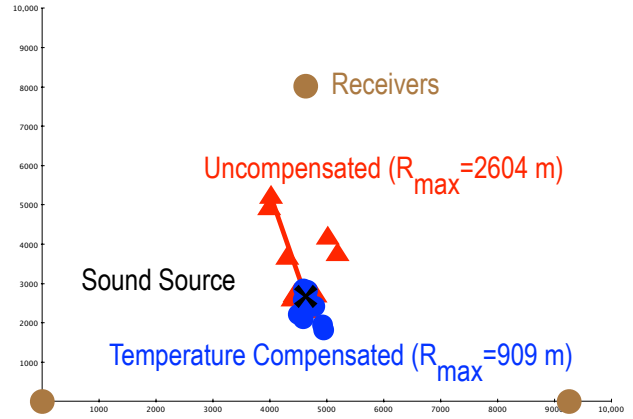


Fig. 1: Example sound localization by compensated and uncompensated data. Symbol key: X=sound source, O=acoustic receivers, triangles=location estimates from uncompensated data, dots=location estimates from temperature compensated data. Note that the uncompensated data have a higher maximum error and variance than the temperature compensated data.

The fourth and final phase corrects the recorded data using the error information, involving

increasing or decreasing the amount of data in each temperature-log-interval proportionally to its frequency error. There are several methods for changing the number of samples in each interval, from simple duplication or deletion of select samples to filter based operations that minimally affect frequency content. The fourth phase was implemented in our case as follows: The temperature-correction profile's format was designed to compare the actual and desired positions of two samples, calculating the difference between their actual interval and desired interval, and then evenly duplicating or omitting samples throughout the interval. This process was applied to the data in 15-minute intervals, using the calculated sample count for each temperature-log interval. On this scale, the assumption that frequency drift is constant over the interval is reasonable given the large thermal mass of the MARU. In cases where alignment of the data from multiple MARUs was necessary, improved results were obtained by applying the temperature correction of frequency to an acoustic synchronization that uses a GPS-timed audio cue.

To evaluate this procedure, three MARUs were assembled and prepared as in the first two phases above. Their recordings were started and the units were placed in a large chest freezer at $2^{\circ}\text{C} \pm 0.5^{\circ}\text{C}$. They were left for 18 days. Periodically, the freezer was opened, and a sound was made to provide a distinct, simultaneous event on each recording. After 18 days, the recordings were terminated. Phases three and four of the above procedure were applied to the recordings, and the results analyzed.

IV. RESULTS AND ANALYSIS

Two synchronization metrics were measured. First, the absolute error between the recorded time of arrival and the expected time of arrival was calculated to evaluate the change in accuracy

of the synchronization. Second, the relative error in time of arrival between units was calculated to evaluate the change in precision of the synchronization. In Table 1, the average absolute error of each unit is given. In Table 2, the average relative error between units is given. This improvement is equivalent to using a TCXO on the ADC board, as the uncertainties are about equivalent.[4]

Average Absolute Synchronization				
	Uncompensated		Compensated	
Chan.	Mean (s)	Std Dev (s)	Mean (s)	Std Dev (s)
1	0.615	0.453	0.426	0.262
2	0.619	0.429	0.508	0.226
3	0.688	0.447	0.396	0.223

Table 1 Average absolute error per channel for all test sounds

Average Relative Synchronization				
	Uncompensated		Compensated	
Chan.	Mean (s)	Std Dev (s)	Mean (s)	Std Dev (s)
1 to 2	0.331	0.207	0.136	0.145
1 to 3	0.970	0.944	0.316	0.229

Table 2 Average relative error between channels for all test sounds

In Fig. 1, the above relative synchronization data were applied to a theoretical, typical, arrayed deployment in which the produced sounds would reach each unit at the same time. A localization algorithm was run on the data to evaluate the practical effect of the synchronization improvement. As can be seen, the temperature compensation algorithm improves the accuracy of the localization by a factor greater than two. The uncompensated locations are incorrect by 981 meters on average, with a standard deviation of 931 meters. The compensated locations are incorrect by 368 meters on average, with a standard deviation of 301 meters.

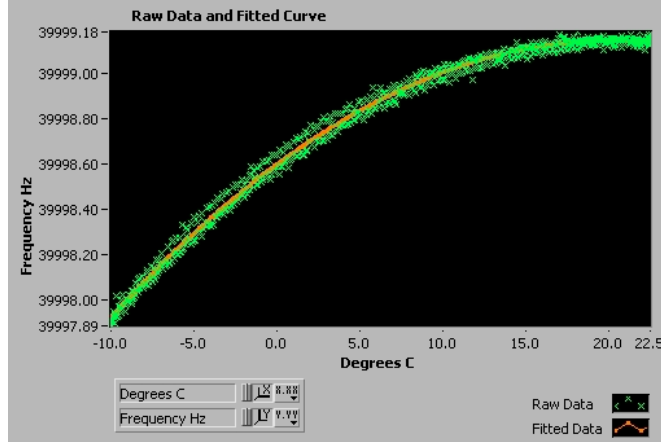


Fig. 2 Example of the recorded system hysteresis of a crystal oscillator for the given temperature range and the fitted curve used in the creation of the frequency drift profile.

V. UNCERTAINTY

The uncertainty in this experiment can be expressed in three parts: the uncertainty of the characterization system, the uncertainty of the temperature recording during deployment, and the residual correction factor for the interpolation phase. In the characterization system, the thermocouple thermometers are the largest source of uncertainty. Second to that is the DMM uncertainty in frequency mode. A minimal amount of uncertainty is introduced by the relay box, and the system noise is relatively low, as the $1/f$ flicker noise is lower at its maximum amplitude than the signal at ~ 40 kHz. Also, as the temperature decreases, so does the Johnson-Nyquist noise, so the thermal noise in the system for the region of interest will be low. The uncertainty of the thermocouple thermometers is ± 0.5 °C[5], and that of the DMM is ± 600 μ Hz[6]. The rated uncertainty of the dataloggers in use in the MARUs for temperature is ± 0.2 °C[7]. However, these were not all tested together at one point in time, and so may be offset from one another. Further characterization against known physical standards is called for in this case. The correction factor makes the time scale slide back and forth by ± 0.5 samples, and thus contributes

an uncertainty of $\pm \frac{1}{2f_s}$.

VI. CONCLUSION

Using this method, the timing uncertainty resulting from thermally induced drift in quartz crystals can be compensated. This compensation method is robust enough to be used for low f_s applications, such as for acoustic recordings and localization, and is an attractive alternative when power or cost constraints preclude the use of furnaced or cut crystals. Finally, the method described gives similar uncertainties to a TCXO or OCXO at lower cost.

ACKNOWLEDGEMENTS

The authors would like to thank Chris Clark and the administrative staff of the Bioacoustics Research Program at the Cornell Lab of Ornithology for supporting this physical research in furtherance of their stated biological goals.

Use of Cosmic Ray Air Shower Products for Synchronization of Underwater Recording Units

Peter Marchetto^{1,2} and Harold Cheyne¹

¹Bioacoustics Research Program, Cornell Lab of Ornithology, Cornell University, Ithaca, NY, USA

²Department of Biological and Environmental Engineering, Cornell University, Ithaca, NY, USA

ABSTRACT— This work explores the potential of using cosmic ray air shower products to synchronize an array of autonomous underwater recorders in post-processing. Because the electromagnetic spectrum below 1 GeV is blocked by the Faraday cage behavior of bodies of water, and ELF-length antennae are not feasible in this application, air shower products offer an attractive alternative for an in-deployment synchronization signal. A test was performed using low-cost ionization detectors in two sealed Marine Autonomous Recording Units (MARUs). The data collected were then analyzed, and candidate events were matched, to demonstrate the feasibility of using these signals to time-synchronize multiple independent devices.

I. INTRODUCTION

Most underwater recording and sensing platforms, including the Marine Autonomous Recording Unit (MARU)[8] lack the capability of synchronizing themselves with other units across an array. Most current methods of underwater sensor array synchronization rely either on GPS clocks through a surface expression with a dedicated antenna, or on carefully orchestrated acoustic pings, which are extremely power-intensive. Power limitations and/or deployment

logistics (e.g., extreme depth) usually preclude having a surface expression for the recorders for GPS. Using an acoustic pinger to generate known acoustic events for synchronization has the disadvantage that neither the underwater recorder's precise position nor the speed of sound between the pinger and the recorder can be characterized well, leaving the post-processing synchronization using the pinger signals error-prone. Out-of-system synchronization methods have been tried with the MARUs, including the end-sync method and in-water tone playback, both of which rely upon an in-situ injected stimulus, and post-processing temperature compensation. [9], [10] All of these methods still leave something to be desired in terms of uncertainty, as the best of them can still only achieve a clock-linked uncertainty of ± 3 ppm.

Most of the electromagnetic spectrum cannot penetrate the ocean: RF above several kHz has a skin depth measured in single meters, and anything above that up to gamma radiation has a relatively short propagation length. Gamma rays can travel some distance in water, but they're easily confused with natural background radiation owing to the presence of naturally radioactive salts in seawater. This leaves the upper end of the energy spectrum, leaving anthropogenic photon sources behind, and delving instead into the realm of cosmic rays.

II. THEORETICAL BACKGROUND

Cosmic rays are actually comprised of a bevy of different elementary particles that are incident on the atmosphere. Most of these are protons have been accelerated at up to about $0.99 c$ by movement through galactic and stellar magnetic fields. Their interaction with the atmosphere creates a cascade of less massive particles that radiates outward from the initial interaction site, while propagating downwards towards the surface of the earth, known as an air shower. Most cosmic rays in the 100 GeV energy range occur with a frequency of about 1/day, have an air shower surface expression on earth of about 10-14 km (depending on incident particle speed),

and a shower interaction depth of up to 15 km below the planetary surface. [11]-[13] This gives extraordinarily good odds that candidate events will happen often enough during a deployment to make them useful for synchronization.

In a worst-case scenario, consider a particle with an energy of 100 GeV, traveling at $.75c$, incident at a very shallow angle through the atmosphere. [11] Given an array nearest-neighbor distance of 10 km, the transit time of the array segment interacting with this air shower will be 44 μsec , which is approximately 0.067 m with a sound speed of 1500 m/sec, or three samples at a sampling frequency of 64 kHz. This gives an average synchronization error for the event of ± 2 samples at $f_s=64$ kHz.

III. METHOD

In this experiment, two MARUs were deployed with an ionization detector in place of their standard hydrophones. The detectors had an 81 VDC nominal power supply comprised of nine 9-volt batteries in series, connected to a 1 k Ω resistor in series with a neon indicator lamp, model 2ML (Visual Communications Co., Poway, CA, USA). [14] A standard monaural 1/8" tip-sleeve jack was added to measure the voltage across the resistor. Whenever ionizing radiation struck the lamp, it would cause a conductive path to be formed within the bulb, allowing a small spike in the current through the resistor. This would then be recorded by the unit's on-board Analog to Digital Converter (ADC), based on the TattleTale Model 8 (Onset Computer, Bourne, MA, USA)[15]. This data was stored on a CompactFlash card, and retrieved after the deployment ended. The two units were first exposed to variable temperature environments for a week, such that their clocks would drift differently, and induce errors in their timing.

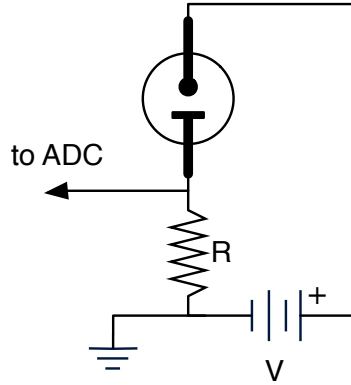


Fig.1 : Schematic of the detector circuit. R is on the order of $\sim 1 \text{ k}\Omega$, while V is below the threshold voltage of the neon bulb, which is on the order of $\sim 90 \text{ VDC}$.

The two units used were then set next to one another with an interstitial distance of $\sim 1 \text{ m}$. The recording delay between the two start times was approximately 45 minutes. The temperature instability in the sample clocks in both encoders was on the order of $>100 \text{ ppm}/^\circ\text{C}$, and the skew before drift was on the order of 173 megasamples.

After the test, both units were unsealed, and their data offloaded. The data was converted from a raw bitstream to AIFF files at 16 bits and 64 kHz sampling frequency. These sound files were then analyzed in Raven 1.5 (Bioacoustics Research Program, Cornell Lab of Ornithology, Ithaca, NY, USA). [16]

IV. RESULTS AND ANALYSIS

A batch detector was run in Raven to find any instances of candidate events. Candidate events were defined as being $>100 \text{ LSBs}$ ($>0.8 \text{ V}$) above the background noise, and less than 0.001 sec in duration. A sample candidate event as seen in Raven is seen in Fig. 2. The same candidate event as a voltage time-series is seen in Fig. 3. The synchrony error of about $68 \mu\text{sec}$ is commensurate with the error expected from clock drift early on in a deployment, as seen in Fig. 4. Two sets of points from the last two weeks of the deployment are seen in Fig. 5, where the clock drift of the two units has brought them to within 41 minutes of each other.

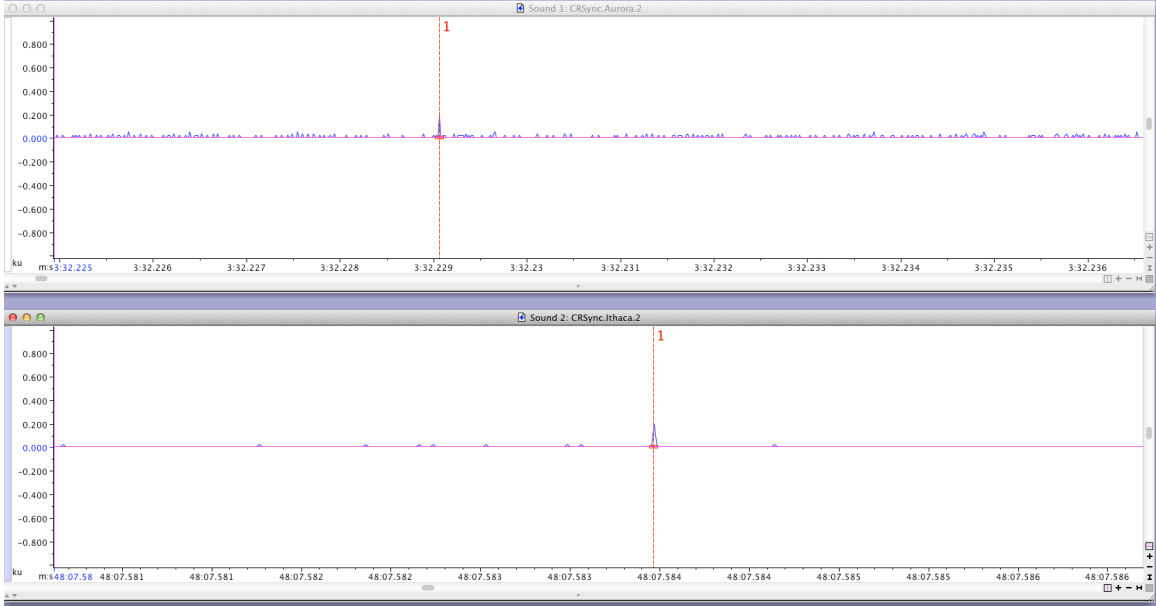


Fig. 2: Temporal offset of two candidate events.

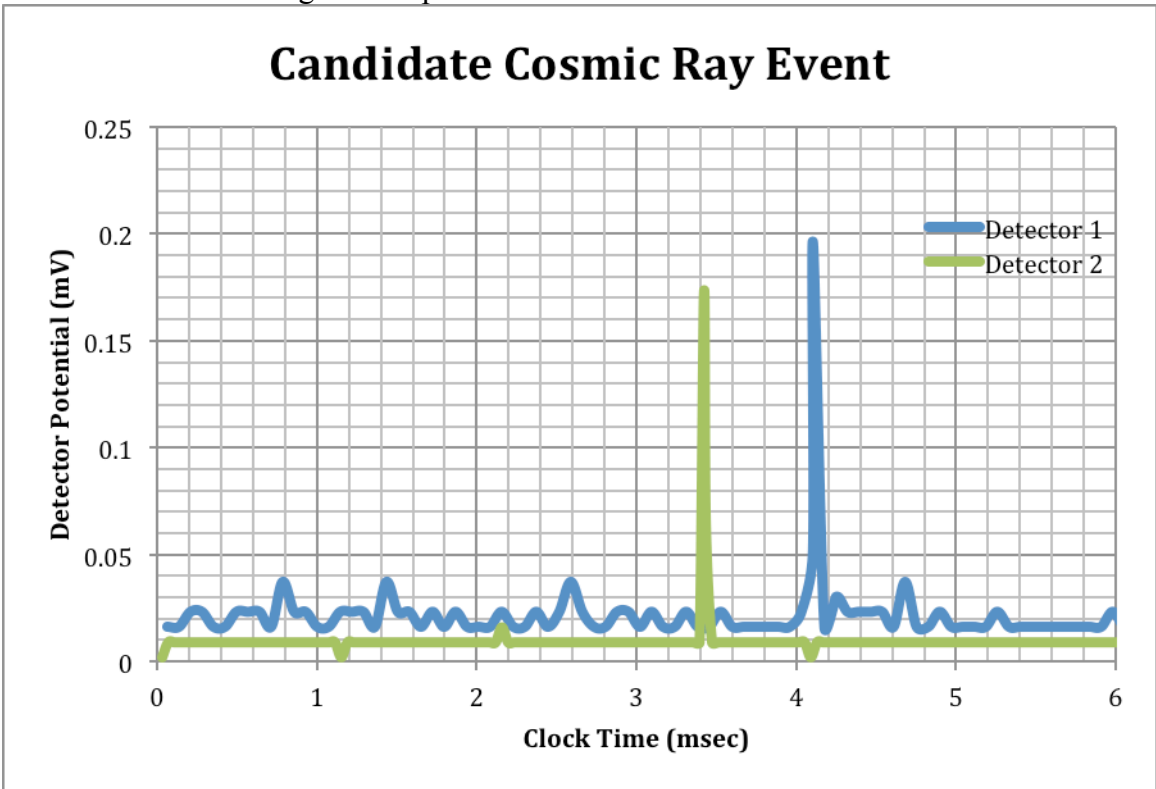


Fig. 3: Finer resolution view of two candidate events aligned from synchronization.

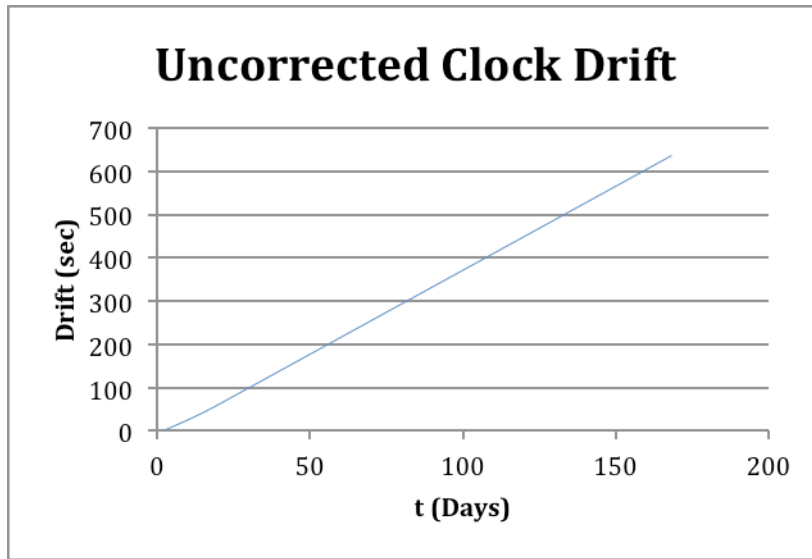


Fig. 4: Typical clock drift from an average MARU sample clock at $f_s=64$ kHz.

As candidate events are recorded on multiple units throughout an array, they create an ensemble of correlations. By using an autocorrelation function with settings on the order of the clock drift expected at a date in the deployment, a series of correlated events can be found, and these then used as anchor points for a stretch/shrink interpolation method. By doing this, the true duration of recordings within the array, and synchrony of the units' clocks might be recovered.

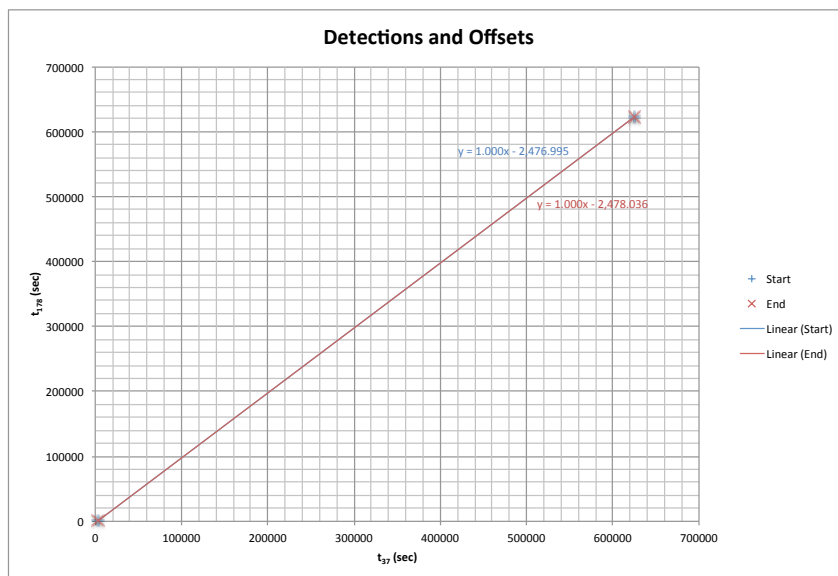


Fig. 5: Detections within the last two weeks of the test. Trendlines from the candidate events show a possible drift of up to 1 sec over the course of one week. The y-intercept is equal to the start delay between the two units, adjusted for clock drift.

Another illustration of the capabilities of this method is in seen in Fig. 5. In this graph, the delay between individual detections is shown, and the independent time scales for each unit are shown on the x and y axes, respectively. By showing the delay, which will vary from clock to clock and unit to unit, along with the time, pairings of candidate events with similar nearest-neighbor times can be found. In this particular case, the candidate events on the first unit are coincident with the first and last candidate events from the second unit. This means that the probability of those being the same event is quite high, and one or both of these pairings could be used for temporal alignment of the recordings.

V. CONCLUSION

The method described above has applications in any scenario where the addition of a clock signal in post-processing is useful. Furthermore, the synchronization signals, if used with a sufficiently precise clock, can be used to trace back the angle of incidence of cosmic rays in this energy band. Finally, the correlation between multiple units across an array, and across multiple candidate events, is more than sufficient to support synchronization for localization using multilateration on sound data.

ACKNOWLEDGEMENTS

The authors would like to thank Robert Koch for his help in deployment, Christopher Tessaglia-Hymes and Raymond Mack for their help in constructing the test units, and Rebecca Ruggles for the use of her dock. This work was internally supported by the Bioacoustics Research Program of the Cornell Lab of Ornithology

Motion in the Ocean: The dynamics of sinking and rising objects through current levels

Peter Marchetto

Bioacoustics Research Program, Cornell Lab of Ornithology, and Department of Biological and Environmental Engineering, Cornell University, Ithaca, NY, USA

ABSTRACT— This paper proposes a predictive algorithm for determining landing and surfacing radii of dropped and floated instruments in water. Particular attention is paid to examples of traversal of multiple current layers.

I. INTRODUCTION

Many methods exist for finding where a drifting object may be on the surface of the ocean or in it[17]-[23], and many methods seem to also exist to explain how the relative forces of water and wind may affect that object's motion while floating. However, when deploying objects that sink to the ocean floor or rise to its surface, it would be helpful to have a means of predicting the landing and surfacing radii. The algorithm described in this paper aims to fix the current dearth of such methods.

VI. DEFINITION OF VARIABLES

A. Inputs

Parameter	Symbol
Float Drag Coefficient	c_{dF}
Float Density (kg/L)	ρ_{sF}
Anchor Drag Coefficient	c_{dA}
Anchor Density (kg/L)	ρ_{sA}
Delay Time (sec)	t_{delay}
Deployment Depth (m)	h
Water Current Velocity (m/sec)	v_{cw}
Wind Speed (m/sec)	v_{ca}
Medium Density (kg/L)	ρ
xy-Plane Cross Sectional Area of Float (m ²)	A_{xyF}
xz/yz-Plane Cross Sectional Area of Float (m ²)	A_{zF}
xy-Plane Cross Sectional Area of Anchor(m ²)	A_{xyA}
xz/yz-Plane Cross Sectional Area of Anchor(m ²)	A_{zA}
Volume of Float (L)	V_F
Volume of Anchor (L)	V_A
Release-to-Recovery Time (sec)	t_{float}
Acceleration Due to Gravity (m/sec ²)	$g=9.81$
Terminal Velocity (m/sec)	τ
Bearing (°)	θ

B. Outputs

Variable	Symbol
Phase 1 xy-Plane Displacement	ξ_{c1}
Phase 2 xy-Plane Displacement	ξ_{c2}
Phase 3 xy-Plane Displacement	ξ_{c3}

VII. ALGORITHM

This algorithm addresses three phases of xy-plane drift while the object is in motion in the z-axis, as seen in Fig. 1.

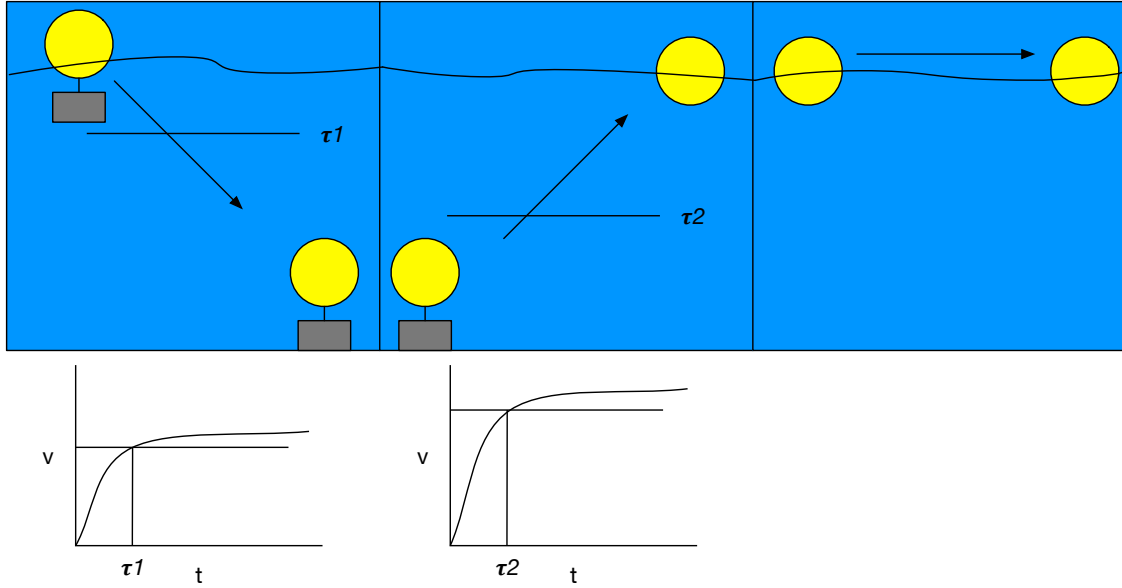


Fig. 1: The three phases of the model: from left to right, sinking with an anchor-float system, detachment and rising of the float from the anchor, and surface drifting of the float by itself.

C. Phase 1: Sinking

First, the terminal velocity of the system is calculated. Since the maximum terminal velocity is what's needed in this model, we treat this as being only the anchor. Thus we find the first terminal velocity, v_{t1} , based on the above parameters:

$$v_{t1} = \sqrt{\left| \frac{\rho_{SA} - \rho}{\rho} \frac{2gV_A}{c_{dSA}A_{xyA}} \right|} \quad (1)$$

Once the terminal velocity is known, the characteristic time, τ_1 , can be calculated. This is the time over which the system experiences a logarithmic acceleration, ending when it reaches v_{t1} .

$$\tau_1 = \frac{v_{t1}}{\frac{c_{dSA} - \rho}{\rho} g} \quad (2)$$

This is then multiplied by the average velocity over the acceleration period, v_{i1} , to give the height of the system at the end of its acceleration:

$$h_1 = v_{i1} \tau_1 \ln(2) \quad (3)$$

When the overall height and the height at which the system ceases accelerating are known, the difference can be found, h_2 , which is the height traversed by the system over the time that it sinks:

$$h_2 = h - h_1 \quad (4)$$

This then leads to the sinking time, t_2 :

$$t_2 = \frac{h_2}{v_{t1}} \quad (5)$$

Meanwhile, the xy-plane, or drift, velocity, v_{xy1} , is found by accounting for the drag coefficients of both the anchor and float parts of the system:

$$v_{xy1} = \frac{\tau_{CF}}{\frac{c_{dF}A_{xF}}{\rho_S V_F} + \frac{c_{dA}A_{xA}}{\rho_{SA} V_A}} \quad (6)$$

Now it's possible to find the displacement from the drop point in the xy-plane, ℓ_{1xy} :

$$\ell_{1xy} = v_{xy1}(t_2 + \tau_1) \quad (7)$$

D. Phase 2: Rising

Next, the terminal velocity of the float alone, v_{t2} , must be found for its journey to the surface:

$$v_{t2} = \sqrt{\left| \frac{\rho_{SF} - \rho}{\rho} \frac{2gV_F}{c_{dF}A_{xF}} \right|} \quad (8)$$

Now it's possible to find the drift velocity, v_{xy2} , of the float alone:

$$v_{xy2} = \frac{\tau_{CF}}{\frac{c_{dF}A_{xF}}{\rho_S V_F}} \quad (9)$$

Then the characteristic time of the float alone, τ_2 , can be calculated:

$$\tau_2 = \frac{v_{t2}}{\frac{v_{t2}}{\rho}} \quad (10)$$

Next, the height at which acceleration stops is calculated, h_3 :

$$h_3 = v_{12}\tau_2 \ln(2) \quad (11)$$

And, now the height that it travels at its terminal velocity can be calculated, h_4 :

$$h_4 = h - h_3 \quad (12)$$

The amount of time that this takes, t_4 , can then be calculated:

$$t_4 = \frac{h_4}{v_{t2}} \quad (13)$$

Finally, the displacement from the anchor on the bottom, ℓ_{2xy} , can be calculated:

$$\ell_{2xy} = v_{xy2}(t_4 + \tau_2) \quad (14)$$

This means that the total displacement from the initial drop point has a magnitude of:

$$\ell_{\text{surface}} = \ell_{2xy} + \ell_{1xy} \quad (15)$$

E. Phase 3: Floating

The time that the float spends on the surface, t_{surface} , can then be calculated from the overall deployment time, and its difference with the rise time:

$$t_{\text{surface}} = t_{\text{float}} - (t_1 + \tau_2) \quad (16)$$

The velocity on the surface, $v_{\text{xy surface}}$, is then calculated by taking a portion of the drift velocity in the water, and of the drift velocity in the air:

$$\left| v_{\text{xy surface}} \right| = \frac{\sqrt{(c_{df}(\rho_a |v_{ca}| \sin \theta_{ca} + \rho |v_{cw}| \sin \theta_{cw}))^2 + (c_{df}(\rho_a |v_{ca}| \cos \theta_{ca} + \rho |v_{cw}| \cos \theta_{cw}))^2}}{\quad} \quad (17)$$

And its bearing from the vector addition of the two velocities:

$$\theta_{\text{surface}} = \tan^{-1} \frac{(c_{df}(\rho_a |v_{ca}| \sin \theta_{ca} + \rho |v_{cw}| \sin \theta_{cw}))^2}{(c_{df}(\rho_a |v_{ca}| \cos \theta_{ca} + \rho |v_{cw}| \cos \theta_{cw}))^2} \quad (18)$$

This can then be used to find the final maximum displacement, ℓ_{3xy} :

$$\ell_{3xy} = v_{\text{xy surface}} t_{\text{surface}} \quad (19)$$

And so the final displacement from the initial drop point can be given by:

$$\ell_{\text{overall}} = \ell_{1xy} + \ell_{2xy} + \ell_{3xy} \quad (20)$$

VIII. MULTI-LAYER FLOWS

In the case of multi-layer flows, the model assumes that there are sharp transitions from one layer to the next. In these cases, the post-terminal velocity term will be taken and vector addition will be necessary to determine the eventual bearing of the sinking or rising device. An example follows below.

F. Two-Layer Flow Sinking

In this scenario, a unit is sinking through two flow layers, one with a flow velocity of $|v_A|$, θ_A , and the other with a flow velocity of $|v_B|$, θ_B . The first layer is h_A deep, while the second is h_B deep, where $h = h_A + h_B$. This means that the first part will be expressed by $h_A - h_I$, where the flow layer is thicker than the terminal velocity distance. From here, it's a matter of simple vector addition to get:

$$|\overline{\ell_{1xy}}| = |v_A t_A| + |v_B t_B| = \frac{\sqrt{(v_A t_A \cos \theta_A + v_B t_B \cos \theta_B)^2 + (v_A t_A \sin \theta_A + v_B t_B \sin \theta_B)^2}}{\quad} \quad (21)$$

and:

$$\theta_{1xy} = \tan^{-1} \frac{(v_A t_A \sin \theta_A + v_B t_B \sin \theta_B)^2}{(v_A t_A \cos \theta_A + v_B t_B \cos \theta_B)^2} \quad (22)$$

As can be seen above, the addition of flow layers can be accomplished fairly easily, and so a multi-layer flow, either on the sinking or rising part of the model, is simple.

IX. PROBABILITY MAPPING

By multiplying the above displacement vectors by a standard Gaussian probability distribution, a

mapping of the Probability Density Function (PDF) of the position of the system can be generated for any time during the modeled interaction. An example can be seen below in Fig. 2.

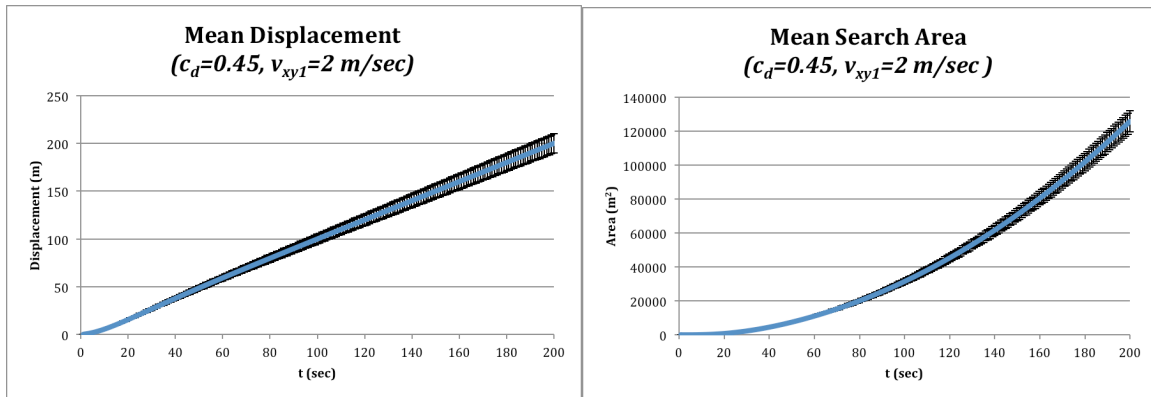


Fig. 2: Mean displacement (left) and mean search area (right) graphs assuming a c_d of 0.45, and a v_{xy1} of 2 m/sec. The error bars show the 1σ points in the gaussian distribution.

X. FUTURE WORK

At this point in time, Inertial Measurement Units (IMUs) have been deployed in two underwater recording units in Cape Cod Bay, MA, USA. These will be recovered soon, and the data from them used with this algorithm to interpret the recorders' sinking and rising characteristics. If this is successful, then an inverse of this method might also be used with IMUs to easily determine current profiles.

XI. CONCLUSION

This algorithm has a number of oversimplifications and perhaps unsupportable assumptions, but is designed as a first step towards understanding these dynamics. Further work is needed, but for the range of instrumentation that currently exists, this algorithm should be able to help bring placement uncertainties back under control.

Characterization of marine autonomous recording units

Peter Marchetto

Bioacoustics Research Program, Cornell Lab of Ornithology, and Department of Biological and Environmental Engineering, Cornell University, Ithaca, NY 14850

pmm223@cornell.edu

Abstract— The Marine Autonomous Recording Unit (MARU) is a common tool used in many underwater passive acoustic surveys. As such, its output data is used for many research questions, from detection and localization of animal calls to measurement of anthropogenic background noise in the ocean. In this paper, the means of characterizing this system to give the most useful, traceable data and its uncertainties is described.

XII. INTRODUCTION

The MARU has been used for over fifteen years to collect recordings of marine mammals, fish, and anthropogenic noise at sea, along with many other sounds. Lately, it has become more apparent that the MARU's weak point is in the uncertainty of the measurements made from its data. This paper is intended to address those uncertainties, and to put forth how each unit is now characterized and its data calibrated.

XIII. TYPES OF UNCERTAINTY

There are two major types of uncertainty to be addressed by this paper: temporal and amplitude. The temporal uncertainty evolves from the method of creating the recording, namely the sample clock. The amplitude uncertainty is generated by several different sources at different points along the signal chain.

1. Temporal Uncertainty

Temporal uncertainty is generated by the behavior of the crystal oscillator that drives the sample clock. In any digital recording system, a sample clock is needed to read out the level received by the Analog-to-Digital Converter (ADC). This clock needs to run at twice the peak frequency that is to be recorded, known as the Nyquist frequency, or $f_s/2$. In most cases, this clock is a quartz crystal that resonates at the frequency desired.

However, quartz clock crystals have a parabolic relationship between their frequency and temperature. They are stable at their quoted frequency (f_0) only when at the temperature at which they were cut (T_0). At any other temperature, they diverge, as in Eq. (1):

$$f(T) = k_1 T^2 + k_2 T + k_3 \quad (1)$$

Where k_1 , k_2 , and k_3 are constants, T is the crystal's temperature, and $k_3 = f_0$ for the particular crystal, such that $f(T_0) = f_0$. Furthermore, each of these three constants has some amount of uncertainty induced by hysteresis. This means that the sampling frequency of a given recorder varies as a function of temperature, and, therefore, if temperature varies with time, then the sampling frequency does, too, as $f_s = f(T(t))$, where $T(t)$ is the record of temperature at a given time, t . For further information, previous work can be found in [24] and [25].

2. Amplitude Uncertainty

The sources of amplitude uncertainty occur at multiple points in the signal chain of the MARU.

The analog signal chain is outlined in fig. 1.

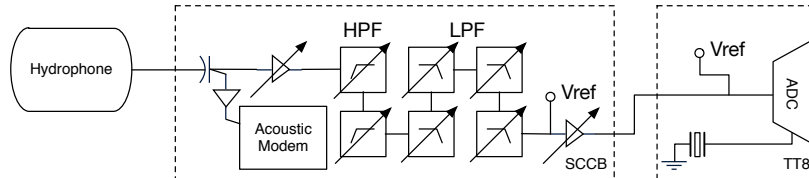


Fig. 1: MARU analog signal chain, including a 2/4 pole adjustable band-pass filter and two separate reference voltage sources. The crystal on the TT8 is the aforementioned source of temporal uncertainty.

Beginning from the input, the hydrophones, all of model 94-SSQ (HTI, Long Beach, MS, USA), have individual sensitivities, M , on the order of -160 dB re 1 V/ μ Pa. These sensitivities are themselves based on input values of supply voltage to the preamplifier, frequency, and temperature, giving a multivariate function, $M(V_{in}, f, T)$, where V_{in} is the input voltage to the preamplifier, f is the frequency of the incoming signal (giving the frequency response), and T , as above, is the operating temperature. The hydrophone is comprised of at least two different types of plastic surrounding a piezoceramic transducer (Navy type IV, lead-zirconium-titanate). Each of these has its own thermal expansion function, and so all three translate to the actual bias pressure upon the transducer, $P_{DC}(T)$, which controls its sensitivity.

Another, non-temperature related effect, is that of having a nearly constant 1 mA current draw from a bank of alkaline batteries with no voltage regulator in line. This means that the potential across the rails of the preamplifier will drop with respect to time, and that the hydrophone will slowly grow deaf over the course of a recording, as $M(V_{in})$ trends towards zero. Given that there are four 20 Ah battery packs in parallel feeding this circuit, this will give a very slow decline, but it's still fast enough to be worth mentioning, as seen in fig. 2.

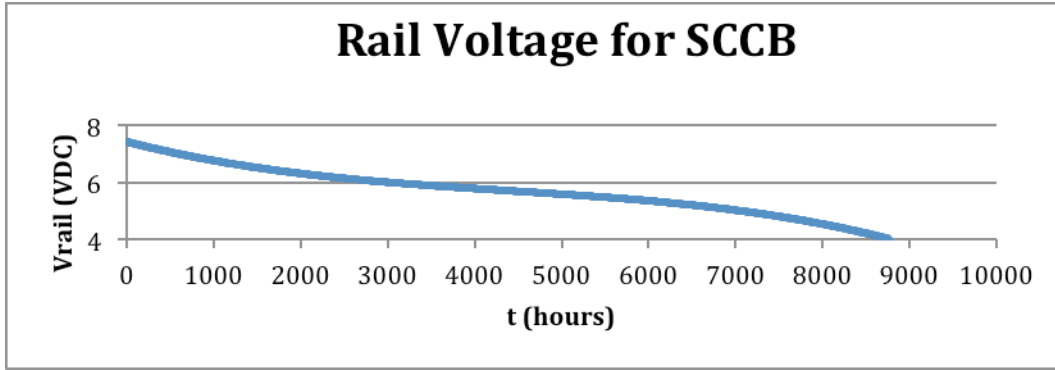


Fig. 2: Rail voltage over time for a standard deployment.

The MARU's Signal Conditioning and Control Board (SCCB) also has a voltage follower that acts to buffer the incoming signal to an acoustic modem, while preserving the signal on the other side of the fork in the signal path, and a large band-pass filter array. This array is comprised of a 4-pole high-pass followed by a 6-pole low-pass, with a preamplifier on either end. All of the units in the current fleet have been observed to have slightly different gain and filter characteristics, despite them supposedly being discretized into certain groups of presets. The gain and filter characteristics, too, are determined by the rail voltage available and the temperature of operation.

The offset voltage, a virtual ground of sorts to reference the signal to, is also generated on the SCCB, and added to the AC component of the output from the filters. Since the rail voltage on the SCCB side of the signal chain is 5 VDC, then, to preserve the dynamic range, the offset voltage is half that, at 2.5 VDC. This is created by a single regulator, whose output has also been found to be temperature dependent, such that it is $V_{offsetSCCB}(V_{in}, T)$.

Further downstream, this signal is piped into the analog input of the TattleTale Model 8 datalogger (Onset, Pocasset, MA, USA). This datalogger is designed to have a 12-bit ADC, and a sensitivity of 1 mV/LSB. This means that its reference voltage of 4.096 VDC is generated by an on-board voltage regulator, which is also temperature dependent, giving $V_{refTT8}(V_{in}, T)$.

In all of the above cases, the unregulated voltage rails will trend towards zero over time, given that the entire system is powered by alkaline batteries on two rails: 7.5 VDC for the SCCB, and 13.5 VDC for the TT8. Temperature is not moderated for the MARU by anything except for a very large heat sink called the ocean.

XIV. CHARACTERIZATION METHODS

For each of the subsystems mentioned above, characterizations were developed. Some of these, such as the acoustic characterizations, were based on known protocols, while others, such as the oscillator characterizations, had to be created from whole cloth.

1. Crystal $f(T)$ Characterization

The frequency of the crystal oscillator is recorded using a 34410A multimeter (Agilent, Englewood, CO, USA) in frequency mode, while the temperature is recorded using a K-type thermocouple connected to a 1048_0 thermocouple input (Phidgets, Calgary, AB, CA). The parabolic regression is done in a custom LabView (National Instruments, Austin, TX, USA) interface program, and its output is stored along with the TT8 serial number in a database locally. The Device Under Test (DUT) is placed into a freezer, allowed to drop to $-5\text{ }^{\circ}\text{C}$, then raised back to $20\text{ }^{\circ}\text{C}$. Again, this method is the same as in [9] and [25].

2. Signal Chain Characterization

The main board of the MARU is placed in a freezer kept at $0\pm 2\text{ }^{\circ}\text{C}$, and connected as seen in fig.

3.

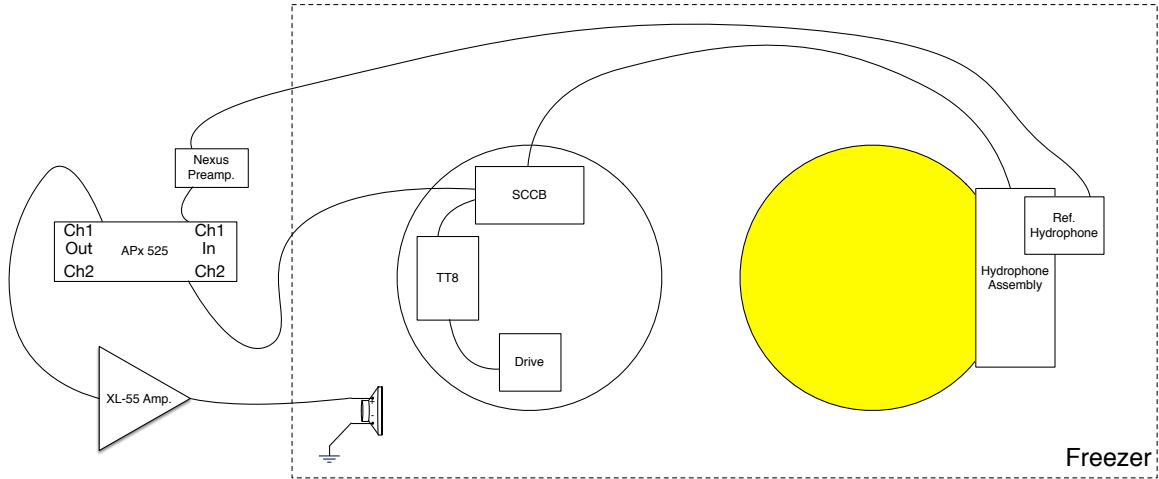


Fig. 3: Test system connection diagram.

The output of the SCCB is split and routed into the TT8 for encoding, as well as into the second input channel of an APx525 audio analyzer (Audio Precision, Beaverton, OR, USA). Stimulus sounds are played from the analyzer through a 55 W amplifier, XL-55 (RadioShack, Fort Worth, TX, USA), and into a TEBM36S12-8/A balanced mode radiator (Tectonic Elements, St. Neots, Cambridgeshire, UK) mounted in a case. The intensity of sound from the radiator is measured by a Type 8103 reference hydrophone (Brüel & Kjær, Nærum, DK) collocated with the DUT's, which is interfaced to the first input channel of the audio analyzer through a Nexus series preamplifier (Brüel & Kjær, Nærum, DK).

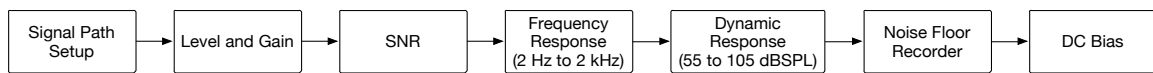


Fig. 4: Test system state diagram.

The recording is usually done at the default settings for the MARU: $f_s=2$ kHz, gain=23.5 dB, HPF=10 Hz, and LPF=800 Hz. A suite of tests is done as seen in the state diagram in fig. 4. The recording is extracted from the on-board memory, and compared to the expected template. The extracted recording and all relevant test data are saved on the test system computer for later analysis. This method was developed from parts of [26], [27], and [28].

XV. RESULTS

1. Crystal $f(T)$ Characterization

For each unit, a temperature compensation curve consisting of a quadratic fit curve from the frequency and temperature data was composed. The three characteristic coefficients, k_1 , k_2 , and k_3 , were exported from this as per the method used in [9]. These were found to have a deviation on the order of ± 2 Hz from their center frequency of 39999.5 kHz. A sample is shown in Fig. 5.

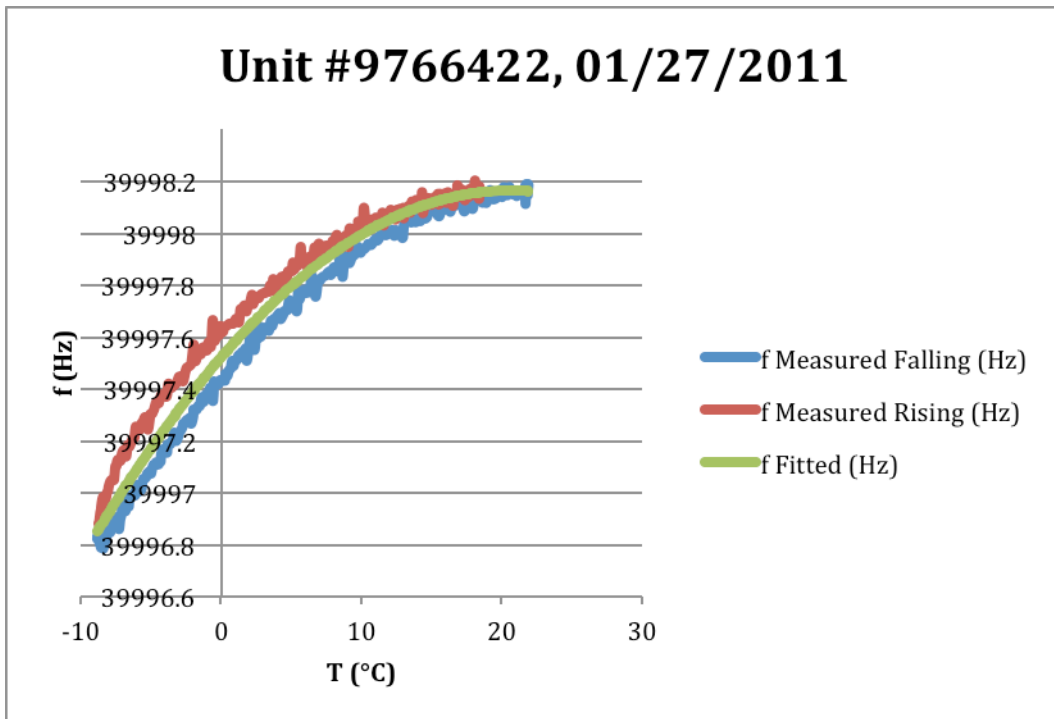


Fig. 5: Sample graph of the $f(T)$ characterization. The frequency of the clock while cooling can be seen in the blue graph, while rising can be seen in the red. The fitted curve of $f(T) = -0.001521T^2 + 0.062669T + 39997.516522$ at $R^2 = 0.974$ can be seen as the green line between them.

2. Signal Chain Characterization

Each unit also had a file generated with its Signal to Noise Ratio (SNR), frequency response, dynamic response, noise floor, and DC offset recorded. These files may be used to inverse filter the data taken from each unit back to the initial input signal, and also can give an idea of what the subsequent ambient and signal sound levels are. Samples of these characterizations are seen in Fig. 6.

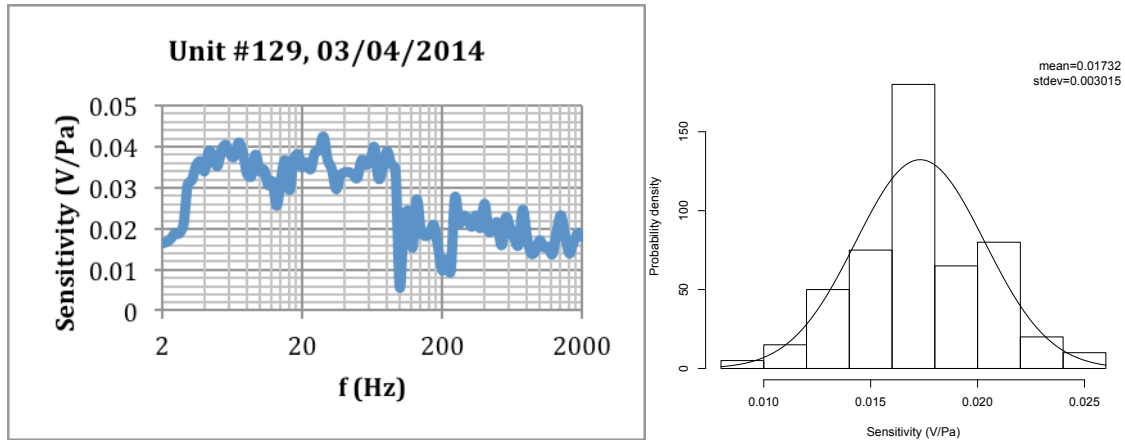


Fig. 6: Sample frequency (left) and dynamic (right) response plots from a unit. The frequency response shows the transfer function at given amplitudes, while the dynamic response shows a histogram of device sensitivity at a 250 ± 2 Hz with probability in ppt.

XVI. CONCLUSION

For the first time, true NIST-traceable characterizations of passive acoustic monitoring devices have been created. These profiles can now be used to confirm and adjust output data and other measurements, and for uncertainty calculations for both localization and sound levels.

XVII. ACKNOWLEDGEMENTS

The author would like to thank his wife and R guru, Katherine Marchetto, for her help in creating figures for this manuscript. The author also wishes to thank Chris Tessaglia-Hymes, Ray Mack, and Harold Cheyne for their help in ironing out the kinks in the calibration systems.

The Sound Pressure Level Observing Transponder (SPLOT): a satellite-enabled sensor package for near real time monitoring

P.M. Marchetto, H.A. Cheyne, C.W. Clark, and D.J. Aneshansley

The authors are **Peter M. Marchetto**, ASABE Member, Graduate Student, **Harold A. Cheyne**, Research Associate, **Christopher W. Clark**, Senior Scientist, of the Cornell Lab of Ornithology, Bioacoustics Research Program, Ithaca, NY, USA, and **Daniel J. Aneshansley**, professor, Department of Biological and Environmental Engineering, Cornell University, Ithaca, NY, USA, where Mr. Marchetto is also a student. **Corresponding author:** Peter Marchetto, B62 Riley-Robb Hall, 111 Wing Dr., Ithaca, NY, 14853; phone: 201.403.5470; e-mail: pmm223@cornell.edu

Abstract— Many in situ sensing applications for the environmental sciences have suffered from a lack of means to communicate information in near-real-time. The monitoring of incidental noise exposure on an individual animal and feasibility of use of a new instrument for such were the focus of this project. The sensor platform described herein could be expanded to sense any number of different environmental variables and could easily be used almost anywhere on the Earth’s landmass. The instrument’s novelty mainly lies in its inexpensive satellite communications and the addition of sound level sensing to a terrestrial animal tag, both of which would allow for quick and easy portability to an agricultural animal monitoring system.

Keywords.

acoustic, animal welfare, environmental impact, noise, noise abatement, noise pollution, remote sensing, sensors

I. INTRODUCTION

Until recently, *in situ* remote sensing has mostly been characterized by a need to retrieve data manually from data loggers, or by in-person checking of environmental variables at given times[29]-[32]. Some instruments have been developed to report from their remote locations using wired or wireless telemetry, but these have been limited by wire length, non-omnipresent telephone service, and wireless link constraints such as FCC regulations on transmission energy or line of sight constraints for FM signals, not to mention power budgets of portable electronics. So far, satellite data transfer has remained slightly over the horizon from most in the environmental sciences, just due to cost, size of equipment, and complexity of satellite communications. This is no longer the case with the advent of the SPOT Connect Personal Locator Beacon (SPOT, LLC, Covington, LA, USA), which is capable of sending up to 41 characters of text back through GlobalStar's satellite network once every ten minutes[33]. Other systems, such as the Icarus Initiative, have yet to come fully online, and logging tags, such as the Daily Diary [34], must be retrieved to have data downloaded. Thus, a commercially available system that can be used today is to be sought.

II. OBJECTIVES

The objective of this study is to test the capabilities of an animal tag to measure at least 4 environmental variable together with location via GPS and determine the methodology for when and how often to transmit this data to a satellite. Sheep will be used as a test animal and sound pressure level, temperature, pressure and relative humidity will be the environmental variable collected. Temperature, relative humidity, and barometric pressure are all used to calculate the acoustic impedance of the air around the instrument and the animal under study.

III. MATERIALS AND METHODS

The SPLOT is designed to send back four different parameters: Sound Pressure Level (SPL), temperature, relative humidity, and atmospheric pressure. The SPL is measured using a model 1133 sound sensor (Phidgets, Calgary, AB, CA), the temperature and relative humidity are measured using a model 1125 T/RH sensor (Phidgets, Calgary, AB, CA), and atmospheric pressure is measured using a model 1115 pressure sensor (Phidgets, Calgary, AB, CA). These four analog measurements are inputs into four of the eight analog inputs on an Arduino microcontroller (Sparkfun Electronics, Boulder, CO, USA). The data from these are collated into a string of less than 41 characters, and are then sent out every ten minutes after a GPS lock is achieved. The GPS interaction and data transmission are moderated by a SatUplink Shield board (Sparkfun Electronics, Boulder, CO, USA)[35], and both GPS and satellite uplink capabilities are ultimately provided by the GPS/SATCOM modem board from a SPOT Connect PLB (GlobalStar/SPOT, LLC, Covington, LA, USA). Figure 1 shows a block diagram of the system, while Figure 2 shows its state diagram .

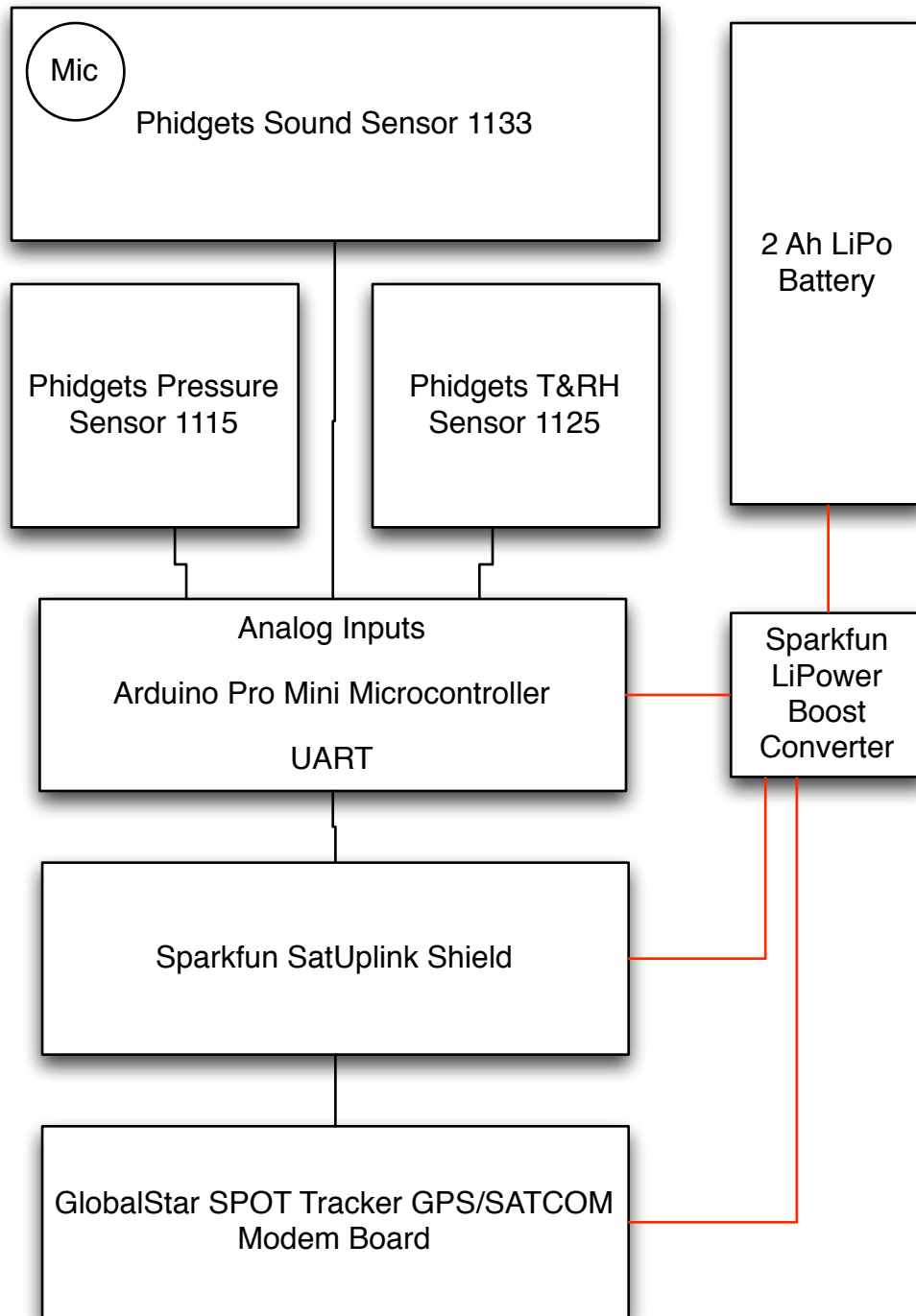


Fig. 1: Block diagram of the SPLOT.

For a test of the system, it was first set outside, stationary at a known location. This allowed for an evaluation of its location uncertainty. This can be seen in Fig. 3, and is about ± 5 m.

The next test of the system was to put it on an animal to be tracked. In this case, sheep

were chosen both due to their availability and the need for a test subject large enough to carry the 2 kg mass of the development board-based prototype device and its protective housing. Several tests were conducted at the Cornell Teaching and Research Farm, in Harford, NY, with animals wearing the device for multiple days. In these tests, the animal was allowed to roam either in a barn or in a pasture depending on the disposition of the flock during those days. All of the animals used in the testing were monitored to see that they stayed with the flock, and didn't stay off on their own due to the added mass of the tag. The tag itself was affixed using a large dog harness in such a way that it would stay in the middle of the animal's back, thus not causing undue stress. This observation of behavior seemed sufficient to make certain that the sheep was not overly stressed, as in Vandenabeele et al. (2014).

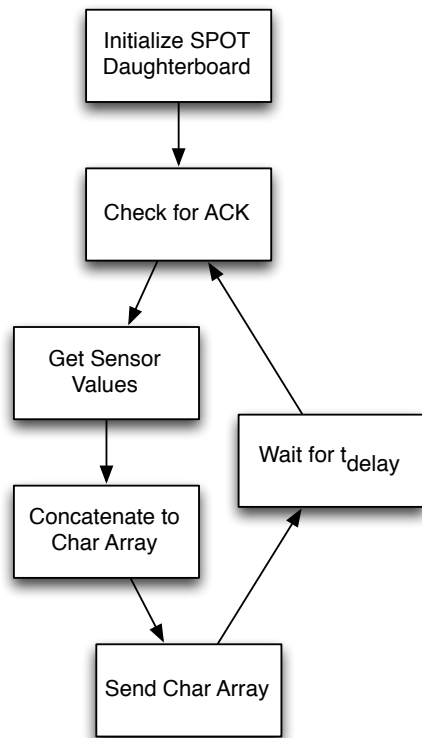


Fig. 2: State diagram of SPLOT v.1 firmware.

IV. UNCERTAINTY

The SPLOT produces a multi-dimensional array of measurement outputs, meaning that there are

several precisions and uncertainties. The precisions of the measurements are shown in Table 2. The uncertainties of each measurement were determined either from manufacturer’s specifications, by calibration with a known standard, or by post-measurement comparison. The uncertainties assessed by these methods are shown in Table 1. The SPL was done by way of a transfer calibration with a NIST-traceable Type 4189 microphone (Brüel & Kjær, Nærum, Denmark) and a loudspeaker on an APx 525 audio analyzer (Audio Precision, Beaverton, OR, USA) in a hemianechoic chamber. The microphone, Device Under Test (DUT), and the speaker were placed at the corners of a 1 m equilateral triangle, and a series of tones at different frequencies and intensities were played.

Measurement	Uncertainty	Units	Method
Position	± 0.00006	°	Post-Comp.
SPL	± 2	dB (A)	Transfer Cal.
T	± 2	°C	Spec.
RH	± 5	%	Spec.
P	± 3.75	kPa	Spec.

Table 1: *Uncertainties of measurements.*

Measurement	Precision	Units
Position	0.00001	°[33]
SPL	0.01	dB (A)[36]
T	0.01	°C[37]
RH	0.01	%[37]
P	0.25	kPa[38]

Table 2: *Precisions and units of reported measurements.*

V. RESULTS AND ANALYSIS

The initial results of this work are very encouraging, as they demonstrate that the environmental parameters in question can indeed be tracked via the SPLOT. Figure 3 shows the data from the stationary test, which indicates that the positional uncertainty is ± 5 m in either axis, and the SPL can be measured to a resolution of 0.1 dBA.

Tracking with the device is possible, as shown in Figure 4, which means that latitude,

longitude, and time are all reported back in an effective manner. Moreover, the data trends over a given period of time, as seen in Figure 5, are not very covariant with each other (most correlations were below $R^2=0.10$), thus confirming that they must be tracked independently.

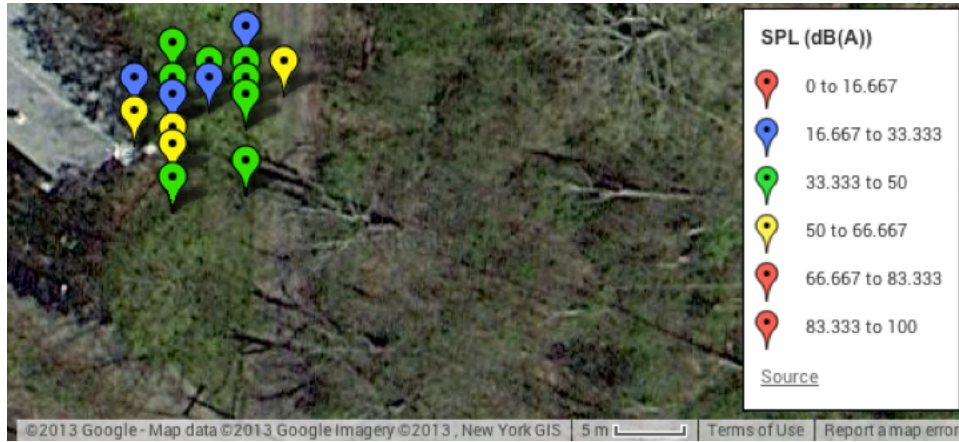


Fig. 3: Preliminary stationary data. Color indicates incident SPL in dBA, as indicated in the legend.

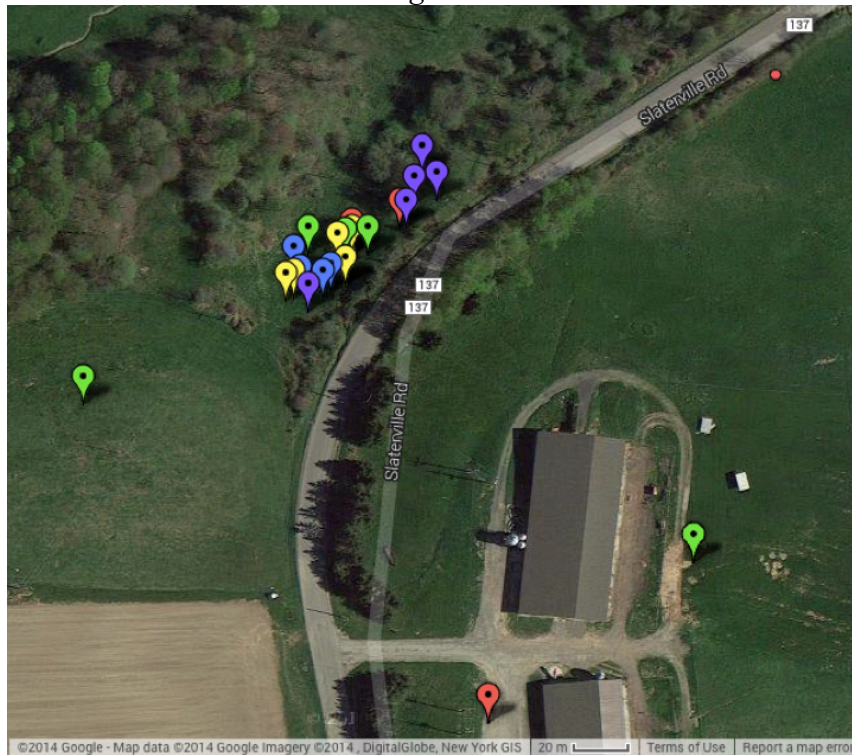


Fig. 4: Track of a sheep from SPLOT waypoints taken every ten minutes. The starting points are in red, and then progress through yellow, green, blue, and purple. During this time, the sheep and its flock were driven from the barn at the bottom of the map to the field across the road where they spent most of their time grazing (and where the highest concentration of points is). The end of the track is on the barn-side of the road where the sheep went after it jumped the fence and crossed the road.

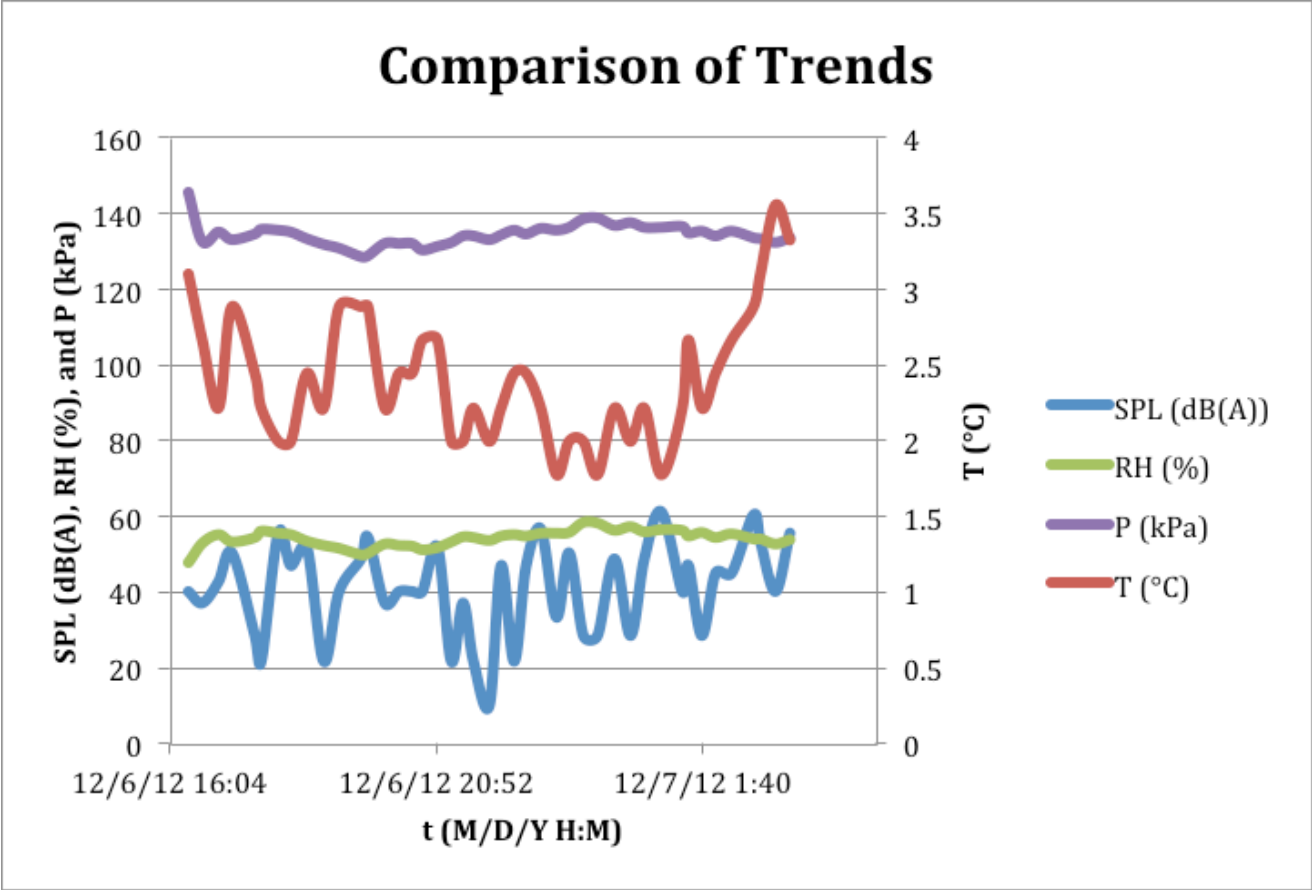


Fig. 5: Comparison of data trends over a reporting period.

VI. CONCLUSION AND FUTURE DIRECTIONS

The SPLOT is an effective, portable tracking platform that may be used virtually anywhere on the globe to measure environmental parameters. Furthermore, its eight ADC inputs make it expandable to additional measurements, such as system power status, light intensity, or other environmental parameters. While 41 characters is not a lot of space, the size and rate of these “data tweets” are sufficient to provide a robust suite of data by which to derive critical information relating an individual’s position and the environmental conditions to which it is exposed.

The SPLOT is still being developed, and the next step in development is to reduce the power budget by powering sensors only as needed, and enabling a larger amount of acoustic data

to be gathered by adding a comb filter to see what frequency bands have the highest amount of acoustic energy. A datalogging version of the device is also under development, which would allow for logging various parameters to on-board memory, to be downloaded upon retrieval. Development also continues on making a single-board solution using a newer, smaller satellite modem, which would allow for use on many more species, having a mass of <0.5 kg.

VII. ACKNOWLEDGEMENTS

The authors would like to thank David Winkler for his advice about environmentally hardened biological sensing systems and putting them on animals, and Al Molnar for his advice and encouragement. Thanks also to Michael Thonney and his staff at the Cornell Teaching and Research Farm for their help with field-testing. Thanks most of all to the ewes who helped by wearing the SPLOT prototype: their part in this work was conducted under Cornell IACUC Protocol 2008-0111, Amendment 0001.

REFERENCES

- [1] “A compact digital recording system for autonomous bioacoustic monitoring,” *The Journal of the Acoustical Society of America*, vol. 108, no. 5, pp. 2582–2582.
- [2] J. Friedt and É. Carry, “Introduction to the quartz tuning fork,” *American Journal of Physics*, 2007.
- [3] J. Vig, “Quartz Crystal Resonators and Oscillators,” *US Army Electronics Technology and Devices*
- [4] Dallas Semiconductor Inc. Maxim Semiconductor Inc., “DS32kHz 32.768kHz Temperature-Compensated Crystal Oscillator,” *datasheets.maxim-ic.com*. [Online]. Available: <http://datasheets.maxim-ic.com/en/ds/DS32kHz-DS32KHZS.pdf>. [Accessed: 11-Jun-2012].
- [5] Phidgets, Inc., “1048 - PhidgetTemperatureSensor 4-Input Product Manual,” *phidgets.com*. [Online]. Available: http://www.phidgets.com/documentation/Phidgets/1048_0_Product_Manual.pdf. [Accessed: 11-Jun-2012].
- [6] Agilent Inc., “34410A/11A 6 1/2 Digit Multimeter,” *cp.literature.agilent.com*. [Online]. Available: <http://cp.literature.agilent.com/litweb/pdf/34410-90001.pdf>. [Accessed: 11-Jun-2012].
- [7] Onset Computer, Inc., “HOBO® Pro v2 user's Manual,” *onsetcomp.com*. [Online]. Available: http://www.onsetcomp.com/files/manual_pdfs/10694-I-MAN-U23.pdf. [Accessed: 11-Jun-2012].
- [8] T. A. Calupca, K. M. Fristrup, and C. W. Clark, “A compact digital recording system for

- autonomous bioacoustic monitoring,” *The Journal of the Acoustical Society of America*, vol. 108, no. 5, pp. 2582–2582, Nov. 2000.
- [9] P. Marchetto, A. Strickhart, R. Mack, and H. Cheyne, “Temperature compensation of a quartz tuning-fork clock crystal via post-processing,” presented at the 2012 IEEE International Frequency Control Symposium (FCS), 2012, pp. 1–4.
- [10] H. Cheyne, A. Strickhart, P. Marchetto, and R. Mack, “System and methods for correcting clock synchronization errors.”
- [11] M. S. Gordon, P. Goldhagen, K. P. Rodbell, T. H. Zabel, H. H. K. Tang, J. M. Clem, and P. Bailey, “Measurement of the flux and energy spectrum of cosmic-ray induced neutrons on the ground,” *Nuclear Science, IEEE Transactions on*, vol. 51, no. 6, pp. 3427–3434, 2004.
- [12] D. K. Bailey, “Abnormal Ionization in the Lower Ionosphere Associated with Cosmic-Ray Flux Enhancements,” *Proceedings of the IRE*, vol. 47, no. 2, pp. 255–266, 1959.
- [13] M. Friedlander and F. Jones, “A thin cosmic rain: particles from outer space,” *American Journal of Physics*, 2001.
- [14] Visual Communications Company, LLC, “Neon Indicator Lamps 7 & 8,” *vcclite.com*. [Online]. Available: http://vcclite.com/_pdf/Neon%20Indicator%20Lamps_7_&_8.pdf. [Accessed: 20-Feb-2015].
- [15] Onset Computer, Inc., “Tattletale Model 8 Installation and Operation Manual,” *onsetcomp.com*. [Online]. Available: http://www.onsetcomp.com/files/manual_pdfs/TT8C_Man.pdf. [Accessed: 03-Nov-2011].
- [16] R. A. Charif and L. M. Strickman, “Raven 1.4 User's Manual,” *birds.cornell.edu*, 2010.

- [Online]. Available: <http://www.birds.cornell.edu/brp/raven/Raven14UsersManual.pdf>.
[Accessed: 20-Feb-2015].
- [17] P. Ailliot, E. Frénod, and V. Monbet, “Long Term Object Drift Forecast in the Ocean with Tide and Wind,” <http://dx.doi.org/10.1137/050639727>, Aug. 2006.
- [18] N. Tsai, “Analysis of a Free-Fall Anchoring System,” *Offshore Technology Conference*, 1971.
- [19] R. Lampitt and M. Burnham, “A free fall time lapse camera and current meter system,” *Deep Sea Research Part A. Oceanographic ...*, 1983.
- [20] N. Rasclé, F. Ardhuin, and E. A. Terray, “Drift and mixing under the ocean surface: A coherent one-dimensional description with application to unstratified conditions,” *Journal of Geophysical Research: Oceans (1978–2012)*, vol. 111, no. 3, p. C03016, Mar. 2006.
- [21] E. Bjerregaard and E. Sorensen, “Forces and Moments on Under Water Bodies, Obtained From Wind Tunnel Tests,” *Offshore Technology Conference*, 1982.
- [22] B. Hackett, Ø. Breivik, and C. Wettré, “Forecasting the Drift of Objects and Substances in the Ocean,” in *Ocean Weather Forecasting*, Springer Netherlands, 2006, pp. 507–523.
- [23] V. Chandrasekhar, W. Seah, and Y. Choo, “Localization in underwater sensor networks: survey and challenges,” ... *ACM International Workshop on UnderWater Networks ...*, 2006.
- [24] P. Marchetto, A. Strickhart, R. Mack, and H. Cheyne, “Temperature compensation of a quartz tuning-fork clock crystal via post-processing,” presented at the 2012 IEEE International Frequency Control Symposium (FCS), pp. 1–4.
- [25] H. Cheyne, A. Strickhart, P. Marchetto, R. Mack, and C. University, “System and

- methods for correcting clock synchronization errors,” no. 13, Apr. 2013.
- [26] P. R. Martin, R. J. Peppin, National Voluntary Laboratory Accreditation Program (U.S.), *Acoustical Testing Services*. 1994.
- [27] “ANSI/ASA S1.15-1997/Part 1 (R 2011) Measurement Microphones — Part 1: Specifications for Laboratory Standard Microphones,” pp. 1–8.
- [28] “ANSI/ASA S1.20-2012 Procedures for Calibration of Underwater: Electroacoustic Transducers,” pp. 1–53.
- [29] S. J. Cooke, S. G. Hinch, M. Wikelski, and R. D. Andrews, “Biotelemetry: a mechanistic approach to ecology,” ... *in Ecology & Evolution*, 2004.
- [30] Y. Ropert-Coudert and R. P. Wilson, “Trends and perspectives in animal-attached remote sensing,” [http://dx.doi.org/10.1890/1540-9295\(2005\)003\[0437:TAPIAR\]2.0.CO;2](http://dx.doi.org/10.1890/1540-9295(2005)003[0437:TAPIAR]2.0.CO;2), Sep. 2008.
- [31] C. Rutz and G. C. Hays, “New frontiers in biologging science,” *Biology Letters*, vol. 5, no. 3, pp. 289–292, Jun. 2009.
- [32] M. Fedak, P. Lovell, B. McConnell, and C. Hunter, “Overcoming the Constraints of Long Range Radio Telemetry from Animals: Getting More Useful Data from Smaller Packages,” *Integr. Comp. Biol.*, vol. 42, no. 1, pp. 3–10, Feb. 2002.
- [33] SPOT, LLC GlobalStar, Inc., “SPOT Connect Datasheet,” *findmespot.com*. [Online]. Available: http://www.findmespot.com/en/docs/SPOT-Connect-Sheet_REV3_July2011.pdf. [Accessed: 28-Nov-2013].
- [34] “Prying into the intimate details of animal lives: use of a daily diary on animals,” 2008.
- [35] Sparkfun Electronics, Inc., “SatUplink Shield,” *sparkfun.com*. [Online]. Available: <https://www.sparkfun.com/products/retired/11088>. [Accessed: 28-Nov-2013].

- [36] Phidgets, Inc., “1133 User Guide,” *phidgets.com*. [Online]. Available:
http://www.phidgets.com/docs/1133_User_Guide. [Accessed: 28-Nov-2013].
- [37] Phidgets, Inc., “1125 User Guide,” *phidgets.com*. [Online]. Available:
http://www.phidgets.com/docs/1125_User_Guide. [Accessed: 28-Nov-2013].
- [38] Phidgets, Inc., “1115 User Guide,” *phidgets.com*. [Online]. Available:
http://www.phidgets.com/products.php?category=3&product_id=1115_0. [Accessed:
28-Nov-2013].